Amplifying the Effects of Contrast Agents on Magnetic Resonance Images Using a Deep Learning Method Trained on Synthetic Data

Alberto Fringuello Mingo, PhD, Sonia Colombo Serra, PhD, Anna Macula, MSc, Davide Bella, PhD, Marco Alì, PhD, Sergio Papa, MD, Fabio Tedoldi, PhD, Marion Smits, MD, PhD, Angelo Bifone, PhD, and Giovanni Valbusa, MSc

Objectives: Artificial intelligence (AI) methods can be applied to enhance contrast in diagnostic images beyond that attainable with the standard doses of contrast agents (CAs) normally used in the clinic, thus potentially increasing diagnostic power and sensitivity. Deep learning–based AI relies on training data sets, which should be sufficiently large and diverse to effectively adjust network parameters, avoid biases, and enable generalization of the outcome. However, large sets of diagnostic images acquired at doses of CA outside the standard-of-care are not commonly available. Here, we propose a method to generate synthetic data sets to train an "AI agent" designed to amplify the effects of CAs in magnetic resonance (MR) images. The method was fine-tuned and validated in a preclinical study in a murine model of brain glioma, and extended to a large, retrospective clinical human data set.

Materials and Methods: A physical model was applied to simulate different levels of MR contrast from a gadolinium-based CA. The simulated data were used to train a neural network that predicts image contrast at higher doses. A preclinical MR study at multiple CA doses in a rat model of glioma was performed to tune model parameters and to assess fidelity of the virtual contrast images against ground-truth MR and histological data. Two different scanners (3 T and 7 T, respectively) were used to assess the effects of field strength. The approach was then applied to a retrospective clinical study comprising 1990 examinations in patients affected by a variety of brain diseases, including glioma, multiple sclerosis, and metastatic cancer. Images were evaluated in terms of contrast-to-noise ratio and lesion-to-brain ratio, and qualitative scores.

Results: In the preclinical study, virtual double-dose images showed high degrees of similarity to experimental double-dose images for both peak signal-to-noise ratio and structural similarity index (29.49 dB and 0.914 dB at 7 T, respectively, and 31.32 dB and 0.942 dB at 3 T) and significant improvement over standard contrast dose (ie, 0.1 mmol Gd/kg) images at both field strengths. In the clinical study, contrast-to-noise ratio and lesion-to-brain ratio increased by an average 155% and 34% in virtual contrast images compared with standard-dose images. Blind scoring of AI-enhanced images by 2 neuroradiologists showed significantly better sensitivity to small brain lesions compared with standard-dose images (4.46/5 vs 3.51/5).

Conclusions: Synthetic data generated by a physical model of contrast enhancement provided effective training for a deep learning model for contrast amplification. Contrast above that attainable at standard doses of gadolinium-based CA can be generated through this approach, with significant advantages in the detection of small low-enhancing brain lesions.

Key Words: diagnostic imaging, deep learning, amplification of image enhancement, contrast media, novel deep learning training strategy, synthetic data

(Invest Radiol 2023;00: 00–00)

Contrast agents (CAs) are commonly used to improve the visibility of anatomical and pathological features in magnetic resonance (MR) scans, thus increasing their diagnostic value. Recommended CA doses have been determined on the basis of efficacy and safety considerations (eg, for gadolinium-based contrast agents [GBCAs], the current standard-of-care suggests a dose of 0.1 mmol Gd/kg). However, several studies indicate that higher doses of CA may be beneficial for detection and evaluation of smaller lesions, or in cases of low CA uptake. Examples include leptomeningeal disease,[1,2] metastatic cancer,[3–8] multiple sclerosis,[9–11] inflammatory demyelinating polyneuropathy,[12] and pituitary adenomas.[13] Moreover, higher CA dose may facilitate diagnosis in specific cases of meningioma or schwannoma.[14]

Administration of larger doses of CA involves substantial deviation from standard-of-care procedures and may have safety implications, particularly in the light of recent findings on gadolinium retention and deposition.[15,16] Although substantial effort has been devoted to the development of more sensitive MR acquisition schemes[17,18] and CAs with higher relaxivity,[19,20] a promising avenue to boost image contrast in CA-enhanced MR scans relies on processing of standard images. To this end, it has been suggested that artificial intelligence (AI) approaches, using deep learning (DL) techniques such as convolutional neural network (CNN) or generative adversarial network (GAN) models, could be used on MR images to recover the contrast of a standard dose of GBCA from a lower administered dose,[21–27] or to generate an amplified "virtual" contrast, corresponding to higher doses than those normally used, from standard contrast images.[28]

A neural network for this purpose is typically build by an encoder-decoder architecture reading as input precontrast and postcontrast acquired images and generating as output an image with higher contrast enhancement. The training procedure involves feeding standard contrast images to the network and comparing the output with ground-truth high-contrast images, while adjusting network parameters to minimize a loss function, composed by 2 pixel wise components (mean absolute error in image and Fourier transform domain) and a VGG-19–based perceptual component.

The performance of DL is strongly dependent on the size and quality of the training data set used to model the data distribution.

Training data sets should be large enough and sufficiently diverse to avoid bias and enable generalization. They should also include data acquired under a variety of different experimental conditions, sometimes outside standard protocols and typical patient populations. Alas, this kind of data sets is not always available or easily attainable. By way of example, training and validating an AI tool for the prediction of stronger image contrast would require a large set of images acquired at CA doses outside the range of recommended ones in patients with lesions of very different type and conspicuity.

Synthetic data are being increasingly used to implement AI applications in the clinical arena[29,30] with the aim of overcoming the scarcity of real-world training data. Synthetic data can be generated from perturbation of real data, or by using physical or AI-driven generative models. Synthetic data can be used to enrich and extend existing data sets, thus improving generalizability and reproducibility of AI approaches, or even to replace real-world data when these are not available.[31,32]

Here, we describe a DL approach based on synthetic training data to boost image contrast in CA-enhanced MR images. Specifically, we leverage a physical model to simulate different levels of MR image contrast from a GBCA, and we apply the resulting data sets to train a CNN (as originally proposed by Lee et al[33]) to predict contrast at GBCA doses several times larger than those used in the clinical practice. Unlike previous work on virtual amplification of image contrast,[28] our method does not require acquisition of data outside the standard of care and dedicated prospective clinical studies, but can leverage standard data sets. This facilitates enormously the development and extension of AI-based contrast-boosting methods to a variety of applications.

We developed and assessed our AI tool within a translational approach in 2 steps. First, in order to test and refine the simulation strategy, we performed a preclinical study in a rat model of glioma in which we collected a full data set comprising both standard (0.1 mmol Gd/kg) and double-dose images. The virtual double-contrast images generated by a neural network trained with synthetic data were quantitatively and qualitatively evaluated against real double-dose images to assess fidelity and to fine-tune model parameters. Moreover, the validity of the approach was assessed against ex vivo histological data.

In a second step, our AI tool was implemented in a retrospective clinical study, where 1990 examinations from patients with a variety of brain diseases were leveraged to generate synthetic images to train the deep network. Quantitative and qualitative analyses of the AI-enhanced images were presented and discussed in terms of potential benefits for detection and evaluation of small lesions in brain conditions such as metastatic cancer and multiple sclerosis.

MATERIALS AND METHODS

Study Design

The purpose of the present study was to train a CNN to virtually double the effects of the CA. To this end, we started from a data set comprising images acquired before CA administration (hereafter named as "pre-CA") and after 0.1 mmol Gd/kg of GBCA (hereafter named "standard"), and applied the well-established theory of MR signal to compute half-dose images. Pre-CA and half-dose images were then used as input to a DL network (see below), whereas standard-dose images were used as ground-truth to train the network to amplify image contrast. See Figure 1 for a scheme of the proposed strategy.

We entertain the hypothesis that, when applied to standard-dose images, the trained network reliably predicts the contrast that would be
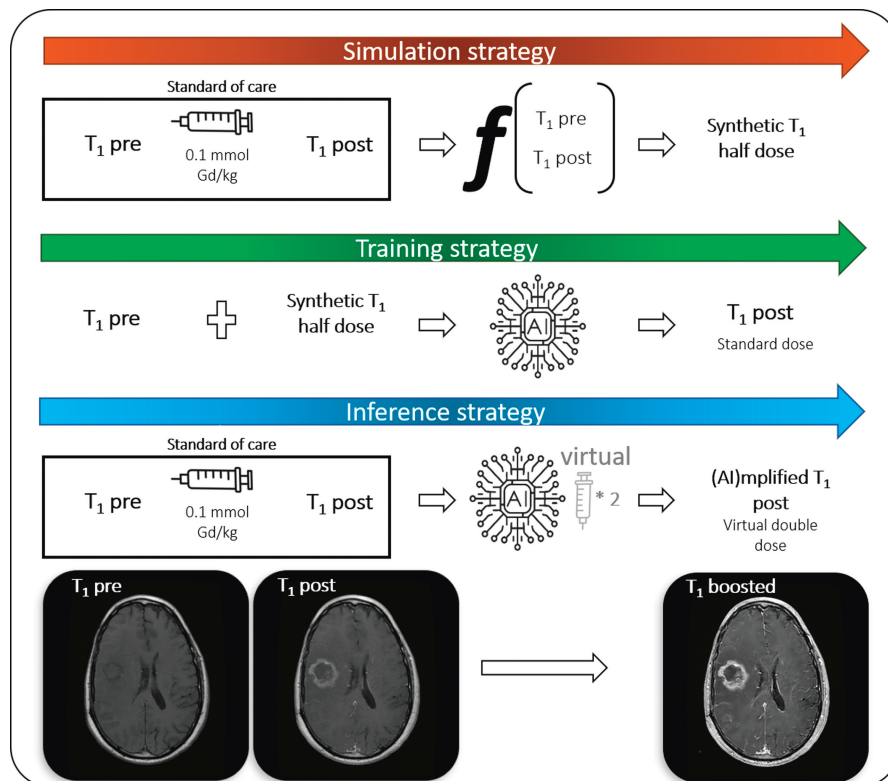
FIGURE 1. Scheme of simulation, training, and inference strategy. The simulation process is based on a physical model to generate half-dose images from precontrast and standard-dose images through analytical computation. The training strategy involves the use of precontrast and synthetic half dose images as input for a CNN, whereas standard-dose images are used as output. The network is trained to predict the contrast for a double dose of CA, relative to the CA used to create input images. Finally, the inference strategy uses the trained model to generate a virtual double-dose image from precontrast and standard-dose images. To illustrate this process, a clinical case is presented in the row of images at the bottom.

generated by a double-dose of CA. This hypothesis was tested experimentally in a preclinical study in laboratory animals, where doses above standard-of-care can be administered to generate ground-truth high-contrast images. Experimental high-dose images in the preclinical model were also leveraged for tuning of hyperparameters. Notably, for the generation of a training data set, our approach requires only pre-CA and standard-dose images, thus making the model applicable in the clinical arena, where data obtained at CA doses above standard-of-care are scarce.

Physical Model

Magnetic resonance image signal in a contrast-enhanced imaging study can be described using a mathematical expression that depends on the following: MR sequence protocol (gradient echo, spin echo, magnetization prepared gradient echo, etc); imaging parameters (echo time [TE], repetition time [TR], and flip angle [α]); tissue parameters (proton density, diamagnetic longitudinal time [T_{10}], transverse relaxation time [T_{20}]); and finally, the local CA's concentration (c), its longitudinal (r_1), and transverse (r_2) relaxivity.

Focusing on spin echo as a representative example, the MR signal equation can be written as:

$$S = S_0 \left(1 - e^{-TR\left(\frac{1}{T_{10}} + r_1 c\right)} \right) e^{-TE\left(\frac{1}{T_{20}} + r_2 c\right)}$$

This expression can be linearized with respect to the local concentration c to its first-order approximation. Then, under the assumption of Tofts model[34–37] that pharmacokinetic processes are linear in this range of doses (between half and full dose) and that local concentration scales linearly with the dose (ie, the local concentration at half dose is one half the concentration at standard dose), the MR signal of half dose images can be calculated as follows:

$$S_{half\ dose} \cong S_{pre} + f(S_0, TE, TR, T_{10}, T_{20}, r_1, r_2)\ c_{half\ dose}$$
$$= S_{pre} + \frac{S_{standard\ dose} - S_{pre}}{c_{high\ dose}}\ c_{half\ dose} = S_{pre} + \frac{S_{standard\ dose} - S_{pre}}{2}$$

where S is the MR signal precontrast, at half dose or standard dose as indicated in the subscripts, and c is the local concentration of CA at half dose or standard dose as indicated in the subscripts.

Data Sets

Preclinical Study

Procedures were conducted according to the national and international laws on experimental animal research (L.D. 26/2014; Directive 2010/63/EU) and under a specific Italian Ministerial Authorization (project research number 384/2021-PR).

Forty-eight male Wistar rats (Charles River Laboratories, Calco, Italy), aged 7–8 weeks (250–300 g body weight), underwent a surgical procedure to induce a glioma by orthotopic injection of C6 rat glioma cells.[38,39] Rat glioma cells were supplied by Sigma Aldrich (ECACC) and cultured in DMEM F-12 medium supplemented with 10% fetal bovine serum, 2 mM glutamine, 100 IU/mL penicillin, and 100 μg/mL streptomycin. For tumor induction, cells were collected, washed 2 times with PBS, and finally a total number of 10^6 cells were resuspended in 10 μL of DMEM F-12.

Rats were subcutaneously injected with carprofen (5 mg/kg) 1 hour before the surgery. Anesthesia was induced with sevoflurane gas and then maintained systemically with Rompun (5 mg/kg) and Zoletil (20 mg/kg). Each rat was then mounted on the stereotaxic apparatus to identify the injection site (0.8 mm anterior, 3.2 mm lateral to bregma and 6 mm ventral to bone). The injection was carried out by using a Hamilton syringe with needle's tip (25 gauge) cut in order to yield more accurate cells release, at a rate of 1 μL/min. The volume was released manually via repeated administrations of 1 μL each 60 seconds. The needle was carefully and slowly removed 15 minutes after the end of the injection to avoid cell dispersion.

In a time window ranging between 7 and 16 days after tumor induction, 44 animals that survived tumor induction procedure and did not show severe clinical signs[40] underwent contrast-enhanced MR imaging for a total of 2/3 sessions. Each examination was recorded 24–48 hours apart.

A total of 121 examinations (acquired at 3 T or 7 T and pooled together) were collected from the 44 animals, each composed of a pre-CA, a standard-dose image, and a double-dose image. For each examination, an additional image corresponding to the administration of half the standard dose ("half dose") was generated applying the simulation strategy described previously.

Magnetic resonance imaging was performed on 2 different preclinical scanners (Bruker Biospin, Ettlingen, Germany): Biospec 47/30 operating at 3 T equipped with a 4-channel rat head surface coil and Pharmascan 70/10 operating at 7 T equipped with a quadrature volume rat head coil. Two different scanners were used to test the effects of field strength on the performance of our AI approach. Each animal underwent 1 or 2 sessions for each scanner for a total of 3 sessions at most.

The contrast-enhanced MR protocol consisted of the acquisition of spin echo T1-weighted images before CA administration, after the

TABLE 1. MRI Acquisition Parameters Used in the Preclinical and Clinical Protocols

Protocol	Preclinical		Clinical
Machine and B_0	Bruker Pharmascan 70/10 Scanner 7 T	Bruker Biospec 47/30 Scanner 3 T	MRI Philips Panorama 1 T, MRI Philips Prodiva CX 1.5 T, MRI GE Signa Twin 1.5 T, MRI Philips Achieva XR 3 T
Modality	T1-weighted	T1-weighted	T1-weighted
Sequence	2D spin echo	2D spin echo	Mainly 2D spin echo
TR	360 ms	400 ms	476 ms (±100 ms)
TE	5.51 ms	14.3 ms	11.9 ms (±3.6 ms)
FOV	32 × 32 mm	32 × 32 mm	—
Matrix size	256 × 256	256 × 256	—
Planar resolution	125 × 125 μm	125 × 125 μm	478 × 478 μm (±143 × 143 μm)
Slice thickness	0.75 mm	1.2 mm	4 mm (±1 mm)

B_0, the static magnetic field; TR, repetition time; TE, echo time; FOV, field of view.
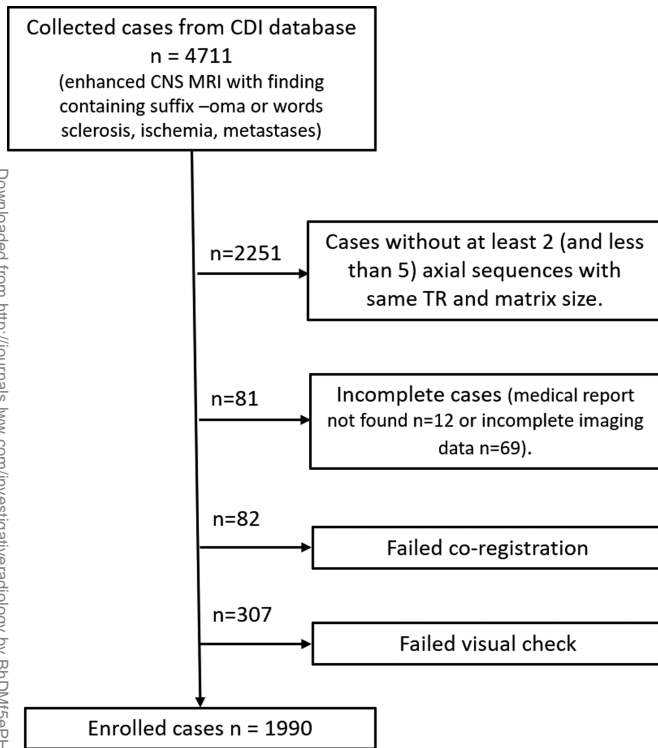
FIGURE 2. Exclusion flowchart for clinical data set.

first intravenous administration through the caudal vein of ProHance (Bracco Imaging, Milan, Italy) at "standard dose" 0.1 mmol Gd/kg and after a second administration of 0.1 mmol Gd/kg. The CA was administered after dilution in saline to a concentration of 100 mM at an injection rate of approximately 1 mL/min. The first postcontrast acquisition started with the first injection of CA. The second postcontrast acquisition started immediately after the end of the first scan, at the time of the second injection. On first approximation, pharmacokinetic effects that may occur in the time window between the administration of the 2 doses were not taken into account, and the second postcontrast acquisition was assumed to correspond cumulatively to a "double-dose" acquisition. This scheme increases statistical power, making it possible a within-subject analysis, thus reducing the number of subjects, according to the principles of 3R.

T1-weighted images were acquired with the parameters reported in Table 1.

Clinical Study

A total of 4711 central nervous system MR imaging examinations, acquired between January 2012 and March 2020 at Centro Diagnostico Italiano (CDI, Milan, Italy; Bracco Group), were considered for inclusion in this retrospective monocentric study approved by the institutional review board (registration number 181/2020). Patients older than 18 years who underwent MR contrast-enhanced brain scans, including a pre-CA and postcontrast image with the same repetition time, axial orientation, and acquisition matrix, were considered for inclusion. The flow diagram (Fig. 2) details the exclusion mechanisms. One thousand nine hundred ninety (of the 4711 collected examinations) with a variety of brain pathologies (eg, meningioma, multiple sclerosis, neurinoma, etc) were included in the study.

The acquisitions were performed using either General Electric or Philips scanners operating at different magnetic field strengths ranging between 1 T and 3 T (MRI Philips Panorama 1 T, MRI Philips Prodiva CX 1.5 T, MRI GE Signa Twin 1.5 T, and MRI Philips Achieva XR 3 T). Most of collected T1-weighted images were 2D spin echo sequences acquired with the parameters reported in Table 1.

Image Preprocessing

Contrast-enhanced images and the corresponding pre-CA acquisitions were geometrically aligned using the SimpleElastix[41] software package with a nonrigid registration procedure. A visual quality check was finally performed through a graphical user interface (GUI) internally developed with PAGE (an open-source program) to exclude the presence of artifacts in the generated images (eg, related to the failure of the coregistration procedure).

Magnetic resonance imaging signal was normalized to have the pre- and half-dose images mapped onto the [0, 1] range, by dividing each image by the maximum value of the synthetic half dose image. Hence, signal in the standard- and double-dose image can exceed the value of 1.

Deep Network Structure

Description of Network. We implemented a U-net like encoder-decoder convolutional neural network as originally described by Lee et al,[33] and as represented in Figure 3. The proposed network consists of an encoder and a decoder. The encoder is a series of 3 convolutional and pooling layers that down-sample the input image while extracting features from it. The decoder is a series of 3 up-sampling and convolutional layers that reconstruct the original image size. Each level of the encoder and decoder path consists of a residual block with 2 sequential 3×3 convolution layer with batch normalization and rectified linear unit (ReLU) activation and a "shortcut" connection consisting of a 1×1 convolution with ReLU and batch normalization. The output of the 3×3 convolution layers is added to the output of the 1×1
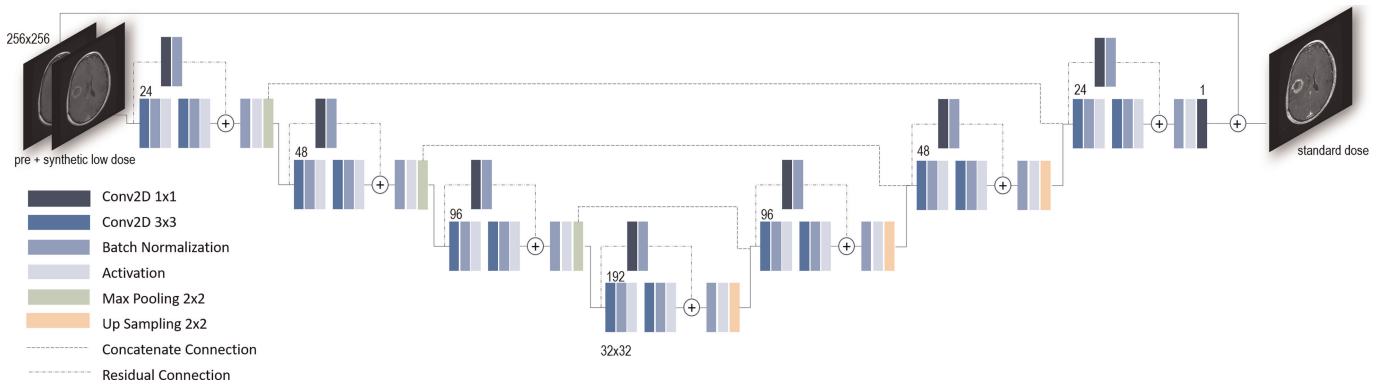

FIGURE 3. Deep learning network architecture used in this work. This model is an encoder-decoder convolutional neural network consisting of a series of 3 encoder steps and a series of 3 decoder steps.

convolution creating the residual connection. In the encoder, each stage is followed by a 2×2 max pooling layer, while 2×2 up-sampling layers are used in the decoder to increase the spatial resolution. Similarly to the original U-net architecture, skip connections are added to connect corresponding levels of the encoder and decoder paths. The number of channels used in each convolution layer is shown in Figure 3. The resolution of the input layer is 256×256. The cost function (described below) compared the prediction and the reference ground-truth full-dose image, which enabled the optimization of the network parameters.

Network Training. Using pairs of pre-CA and simulated half-dose images as input and standard-dose images as ground-truth, the network was trained to predict standard-dose images.

The data set was split in training set (70%), validation set (20%), and test set (10%) to train and validate the DL model. Data augmentation, consisting of rotations, flips, was applied to images of the training set to avoid overfitting and ensure the robustness of the model. A key step in the data augmentation is the adjustment of noise levels to be added to half-dose images to match realistic signal-to-noise and contrast-to-noise levels. To this end, we added normally distributed noise with zero mean and tunable standard deviation (SD) to the simulated images. Normally distributed noise was added, rather than Rician noise, since Rice distribution approaches a Gaussian one at sufficiently high signal-to-noise ratio (SNR) (>2).[42] Since the level of added noise affected the performance of the network, this parameter was treated as hyperparameter.

Stochastic gradient descent and back-propagation were used to optimize the network weights and bias. A 3-component composite loss was used as cost function: mean absolute error (MAE), MAE in the Fourier transform space, and the perceptual loss[43] based on the VGG-19[44] network pretrained on the ImageNet data set and cut at the fourth pooling layer. To match the size of our input with that of VGG-19 network (ie, 3 channels input layer, being trained on RGB images) for each image a 3 channels tensor is created by repeating the grayscale image 3 times. The 3 components of the loss were normalized to balance their weight during training. The normalization procedure consisted of training a network with only one loss component and measuring its mean

value. This mean value was then used to normalize each loss component so that the mean value was set to one. Then, 3 weights were included in the loss function ("a," "b," "c") to modify the relative contribution of each component and to study their effect on the final image quality (IQ). Specifically, the following hyperparameters were subjected to the tuning process: weight of MAE as pixelwise loss component ("a" = 0.5, 1 or 2) and weight of perceptual loss component ("c" = 1, 2, or 5). Similarly, different values of noise SD (ie, 0.0075, 0.01, 0.015, 0.03) were investigated. For each hyperparameter setting (weight of loss components and SD of noise), 5 repetitions of training and testing were carried out after shuffling training, validation, and test data sets. Training was performed with 250 epochs of stochastic gradient descent using ADAM as optimizer with learning rate 0.01 and decay 0.001.

Each trained network was then applied to predict virtual double-dose images using pre- and standard-dose images as input.

Preclinical Evaluation

Similarity of virtual double-dose and standard-dose images against real double-dose images was assessed using peak SNR (PSNR) and structural similarity index (SSIM),[45,46] respectively, a measure of voxel-wise differences (errors) and nonlocal structural similarity. The metrics were computed for both standard-dose images and the virtual double-dose images against the ground-truth, that is, the experimental double-dose image, to study the similarity improvement obtained by the CNN. Data are shown as average values ± standard error. The significance of statistical difference was assessed by a Student *t* test.

Clinical Evaluation

As detailed in Table 2, 2 evaluation studies were performed: the first one aimed at quantitatively assessing the increment of contrast-to-noise ratio (CNR) and lesion-to-brain ratio (LBR), and the second one aimed at qualitatively scoring the visibility of small lesions.

Study 1. For the quantitative and qualitative evaluation of model performance, a subset of 60 patient scans were randomly selected and included in the test set: 22 males and 38 females; mean age, 56 ± 15 years (min = 27, max = 81 years); scanners: MRI Philips

TABLE 2. Description of the Clinical Evaluation Studies

Aspect	Study 1	Study 2
Rationale	To quantitatively assess the increment of CNR and LBR and to qualitatively score DC, CE, AS, and IQ on a 5-point Likert scale	To qualitatively score, the visibility of small lesions on a 5-point Likert scale
Image data set presented to radiologist	A total of 60 patients (for a total of 120 cases/images: 60 true standard dose and 60 virtual double dose) were randomly selected and then included in the present study	A total of 30 patients (for a total of 60 cases/images: 30 true standard dose and 30 virtual double dose) were randomly selected and then included in the present study
Pathologies included	• Meningioma (n = 10) • Multiple sclerosis (n = 10) • Glioblastoma (n = 10) • Astrocytoma (n = 10) • Metastases (n = 10) • Angioma (n = 10)	• Metastases (n = 15) • Active multiple sclerosis (n = 15)
Readers numbers	2 board-certified neuroradiologists (I.L.T. and M.P. with 19 and 1.5 years of experience, respectively) not blinded to image source dose (ie, standard dose or virtual double dose)	3 board-certified neuroradiologists (N.C., C.D.G., and G.S. with 40, 44, and 47 years of experience), respectively, blinded to the image source dose (ie, standard dose or virtual double dose).
Question asked to radiologists	• During the quantitative evaluation: to place on each case a first ROI in the largest homogenous enhancing area of the lesion and a second ROI in the contralateral cerebral parenchyma (avoiding large blood vessels) • During the qualitative evaluation: to grade for each case DC, CE, AS, and IQ on a 5-point Likert scale	To qualitatively grade for each case visibility, degree of delineation and brightness of small enhancing structures on a 5-point Likert scale
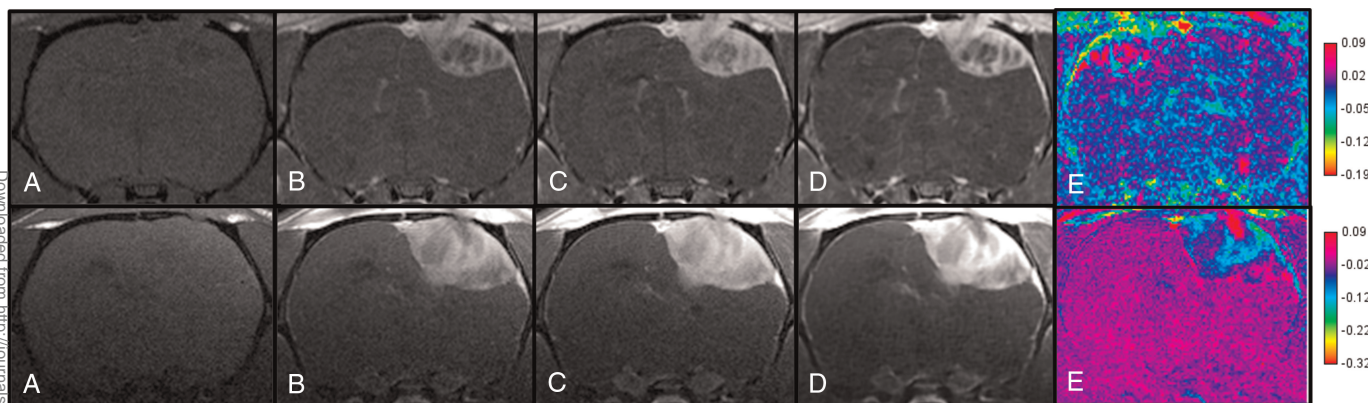
FIGURE 4. Representative example of pre-CA (A), standard-dose image (B), real double-dose image (C), and virtual double-dose image (D), and difference image between real double-dose and virtual double-dose (E) from an examination acquired at 7 T (top row) and 3 T (bottom row).

Panorama 1 T (n = 11), MRI Philips Prodiva CX 1.5 T (n = 27), MRI GE Signa Twin 1.5 T (n = 19), and MRI Philips Achieva XR 3 T (n = 3); even distribution of pathologies (meningioma [n = 10], multiple sclerosis [n = 10], glioblastoma [n = 10], astrocytoma [n = 10], metastases [n = 10], angioma [n = 10]). A total of 120 (60 true standard dose and 60 virtual double dose) cases were presented to 2 board-certified neuroradiologists (I.L.T. and M.P. with 19 and 1.5 years of experience respectively). During the quantitative evaluation, the readers independently placed the first region of interest (ROI) in the largest homogenous enhancing area of the lesion and a second ROI in the contralateral cerebral parenchyma (avoiding large blood vessels). The percentage variation of CNR and LBR of virtual double dose with respect to standard dose was computed for each case with at least 1 enhancing lesion, according to the formulae:

$$CNR = \frac{SI_{lesion} - SI_{brain}}{SD_{brain}}$$

$$LBR = \frac{SI_{lesion}}{SI_{brain}}$$

where SI_{ROI} and SD_{ROI}, respectively, denote the average signal intensity (SI) and its SD in a given ROI (where ROI = lesion, brain). Data are presented as average values ± standard error. During the qualitative evaluation, the readers independently graded diagnostic confidence (DC), clarity of the enhancement (CE), artifact suppression (AS), and IQ on a 5-point Likert scale. Average scores and related 95% confidence intervals were both calculated across readers and type of the image.

Study 2. In a second run of clinical evaluation, the original standard-dose images and the virtual double-dose images were qualitatively evaluated by neuroradiologists N.C., C.D.G., and G.S. with 40, 44, and 47 years of experience, respectively, blinded to the image source. The readers

independently graded visibility, degree of delineation, and brightness of small enhancing structures (larger diameter on average 3.54 ± 1.05 mm; min = 1.04 mm and max = 5.47 mm) on a 5-point Likert scale on 15 cases of metastases (larger diameter on average 3.70 ± 1.26 mm; min = 1.04 mm and max = 5.47 mm) and 15 cases of active multiple sclerosis (larger diameter on average 3.37 ± 0.81 mm; min = 2.33 mm and max = 5.12 mm). Average score across readers and type of the image was computed using 2-tailed *t* test, with a 5% level used for confidence intervals and statistical significance.

RESULTS

Preclinical Results

Figure 4 shows representative examples of experimental pre-CA, standard-dose, and double-dose images compared with AI-generated virtual double-dose images for 2 subjects at 2 different magnetic field strengths (7 T, top row, and 3 T, bottom row). At both fields, virtual double-dose image contrast is substantially enhanced compared with that of standard-dose images, with good delineation of lesion boundaries and tumor heterogeneity in qualitative agreement with the experimental double-dose images. The enhancement of the virtual double-dose image contrast is also apparent in the lateral ventricles and in cortical blood vessels.

The lesions displayed in Figure 4 are characterized by well-defined hyperintense rims. In contrast, Figure 5 presents MR images of a tumor infiltrating subcortical areas, where lower CA uptake makes it difficult to identify tumor boundaries in the standard-dose image (Fig. 5B). Visual inspection of real and virtual double-dose contrast (panel "c" and "d," respectively) shows substantial enhancement of CNR in brain regions away from the point of implantation. Importantly, histological examination of postmortem tissue demonstrates correspondence of virtual contrast with neoplastic tissue in the infiltrated regions. Additional illustrative comparisons of real and virtual double-dose contrast
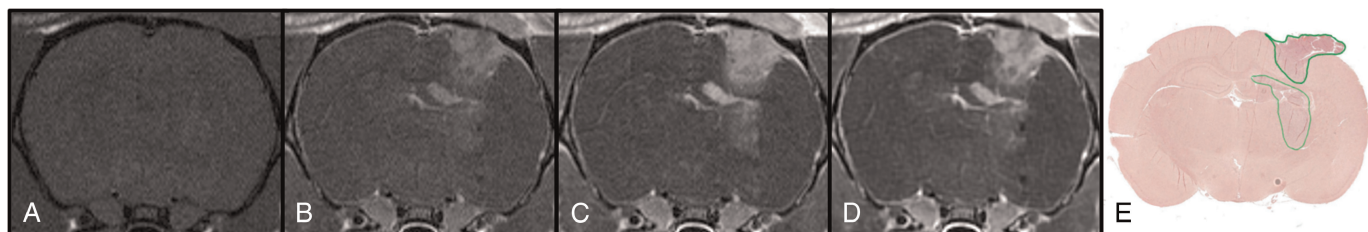
FIGURE 5. Representative example of pre-CA (A), standard-dose image (B), real double-dose image (C), virtual double-dose (D), and histology (E).
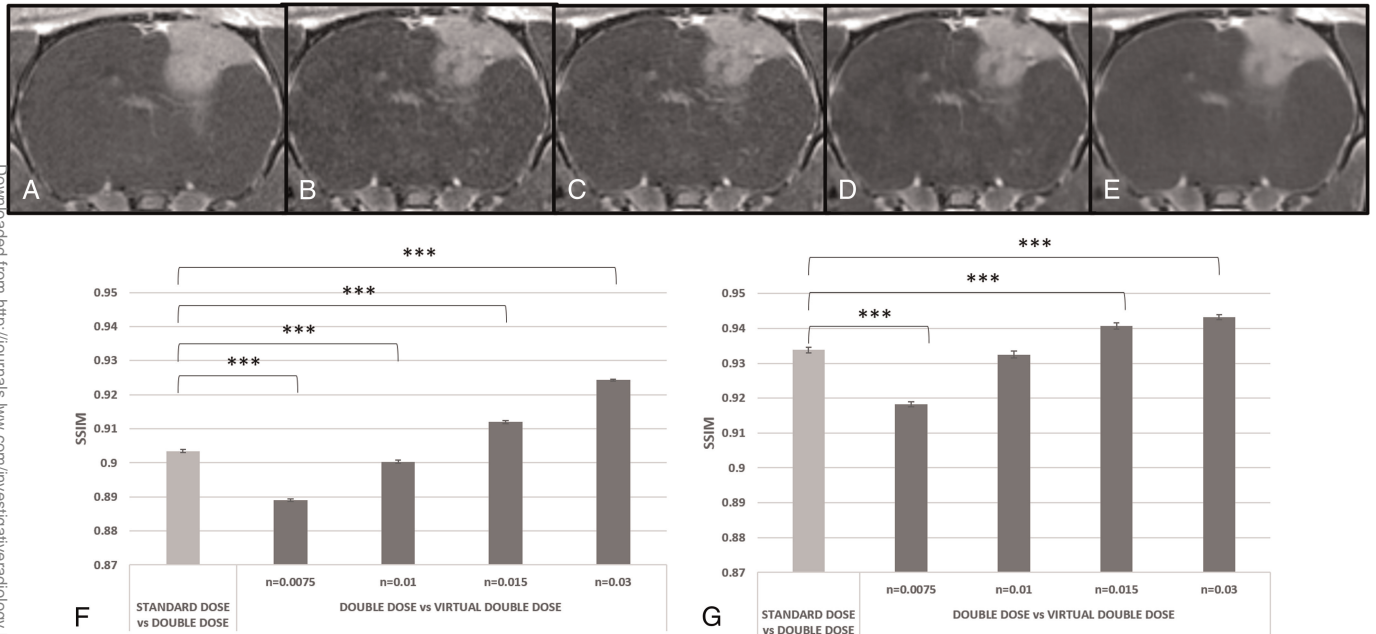
FIGURE 6. Representative example of double-dose image (A), virtual double-dose with noise 0.0075 (B), 0.01 (C), 0.015 (D), and 0.03 (E). SSIM at 7 T (F) and SSIM at 3 T (G). *P < 0.05. **P < 0.01. ***P < 0.

images with histological slices are reported in the Supplementary Material section, http://links.lww.com/RLI/A839.

Focusing on CNN optimization, as described in the Methods section, a small albeit appreciable influence of the weights "a," "b," and "c" was observed (up to 1 dB and 0.5 percentage points for PSNR and SSIM, respectively). Parameters were tuned to increase metrics values of double virtual dose against acquired virtual dose as much as possible. The best result was obtained setting "a" = 0.5 and "c" = 1. The second best results were obtained with "a" = 2 and "c" = 5.

The effect of the noise level is shown in Figure 6, where representative images at increasing noise are reported, as well as a quantitative evaluation based on SSIM. The SSIM was chosen as a metric because it is known to better represent changes in structural information compared with pixel-wise metrics based on absolute errors (such as MSE or PSNR). According to SSIM, the higher the noise, the higher the similarity between acquired and virtual double dose. Visually, at low noise level, the image shows a texture that differs from ground-truth, showing artificial fluctuations of gray levels in the healthy brain parenchyma. At increasing noise fluctuations, results smoothed up to a slightly over blurring for the highest values. The best compromise appears to be the intermediate levels of noise equal to 0.015 for both magnetic field strengths, for which the SSIM values are higher than those obtained with standard dose, and at the same time the blurring is moderate.

After model optimization, quantitative comparison of the experimental and virtual double-dose images was performed on a test data set comprising 13 randomly selected subjects. We used 2 different metrics, PSNR and SSIM, and results were averaged over 5 repetitions of training, shuffling training, validation, and test sets. Figure 7 shows the summary statistics across all subjects included in the test sets for both indices at 3 T and 7 T. It should be noted that the metrics were conservatively computed over the entire image, without prior segmentation of the tumor lesion. Virtual double-dose images show high degrees of similarity to real double-dose images for both PSNR and SSIM (29.49 dB and 0.914 at 7 T, respectively, and 31.32 dB and 0.942 at 3 T) and highly significant improvement over standard-dose images at both field strengths (light gray bars).
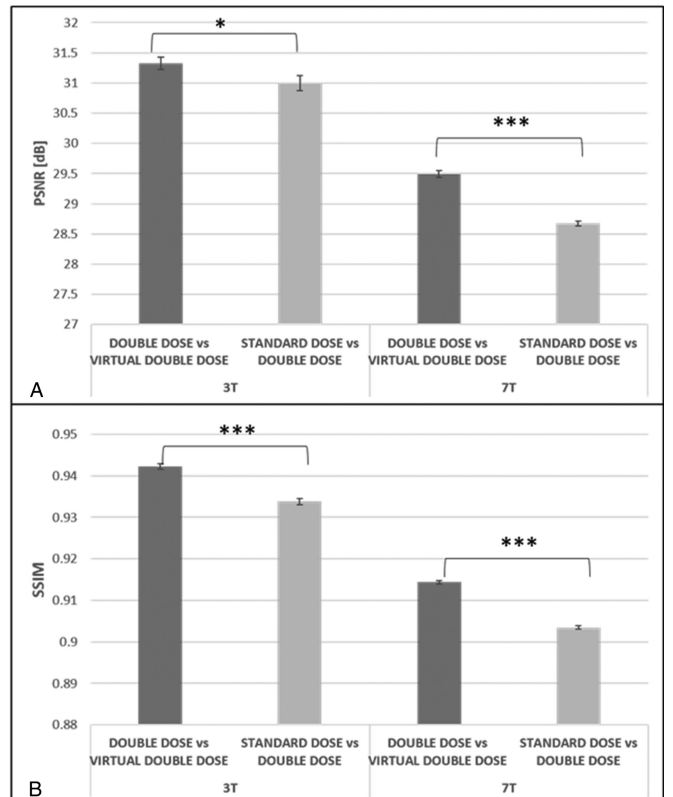
FIGURE 7. Evaluations using quantitative nonsubjective similarity metrics (PSNR [dB] panel A and SSIM panel B) of acquired standard-dose and virtual double-dose compared against acquired double-dose ground-truth on testing data sets. *P < 0.05. **P < 0.01. ***P < 0.

Clinical Results

The network architecture and training procedures that were optimized and validated on the preclinical data set were subsequently applied to a large set of clinical data comprising a variety of brain conditions. Examples of representative cases are reported in Figure 8, where experimental pre-CA and standard-dose images are compared with virtual double-dose ones. Consistent with the preclinical findings, virtual double-dose contrast improves delineation of lesion boundaries and enhances tumor texture compared with standard-dose images, while leaving bright the pre-CA T1 perilesional hyperintense signal. Strong contrast enhancement is also observed in blood vessels, which appear as prominent features in the virtual double-dose contrast images.

The virtual double-dose images were quantitatively and qualitatively evaluated in 2 reading studies, against the original standard-dose acquisition.

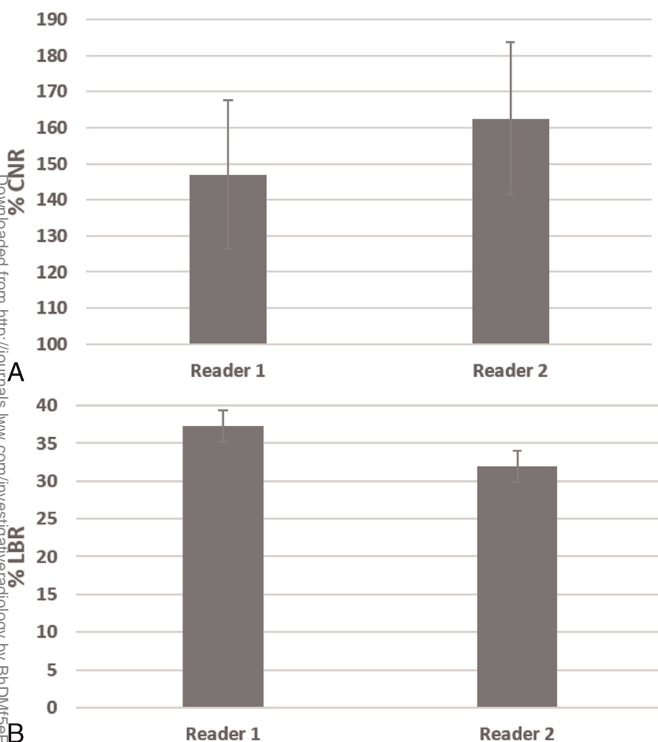The quantitative assessment of the degree of the amplification of virtual double-dose contrast images was evaluated for a subset of 60 patients with various brain pathologies. Results are summarized in Figure 9. The percentage gain in CNR (virtual double dose contrast vs standard dose) and LBR are shown in Figure 9A and Figure 9B, respectively, for the ROIs selected by 2 independent expert readers. Contrast-to-noise ratio and LBR are consistently increased by an average 155% and 34%, respectively, with no significant differences for the 2 readers. The qualitative scores assigned by the 2 neuroradiologists indicated that the CE is maintained acceptable to good for both standard dose and virtual double dose according to reader 1 and increased by 0.5 points in virtual double dose with respect to standard dose according to reader 2 (see Table 3). Both the 2 readers perceived also DC, IQ, and AS not compromised in the virtual double-dose image with respect to that of the standard-dose image. The average qualitative score and the related confidence of interval exhibit a perception acceptable to good for the virtual double-dose contrast as well as for standard-dose image (see Table 3).
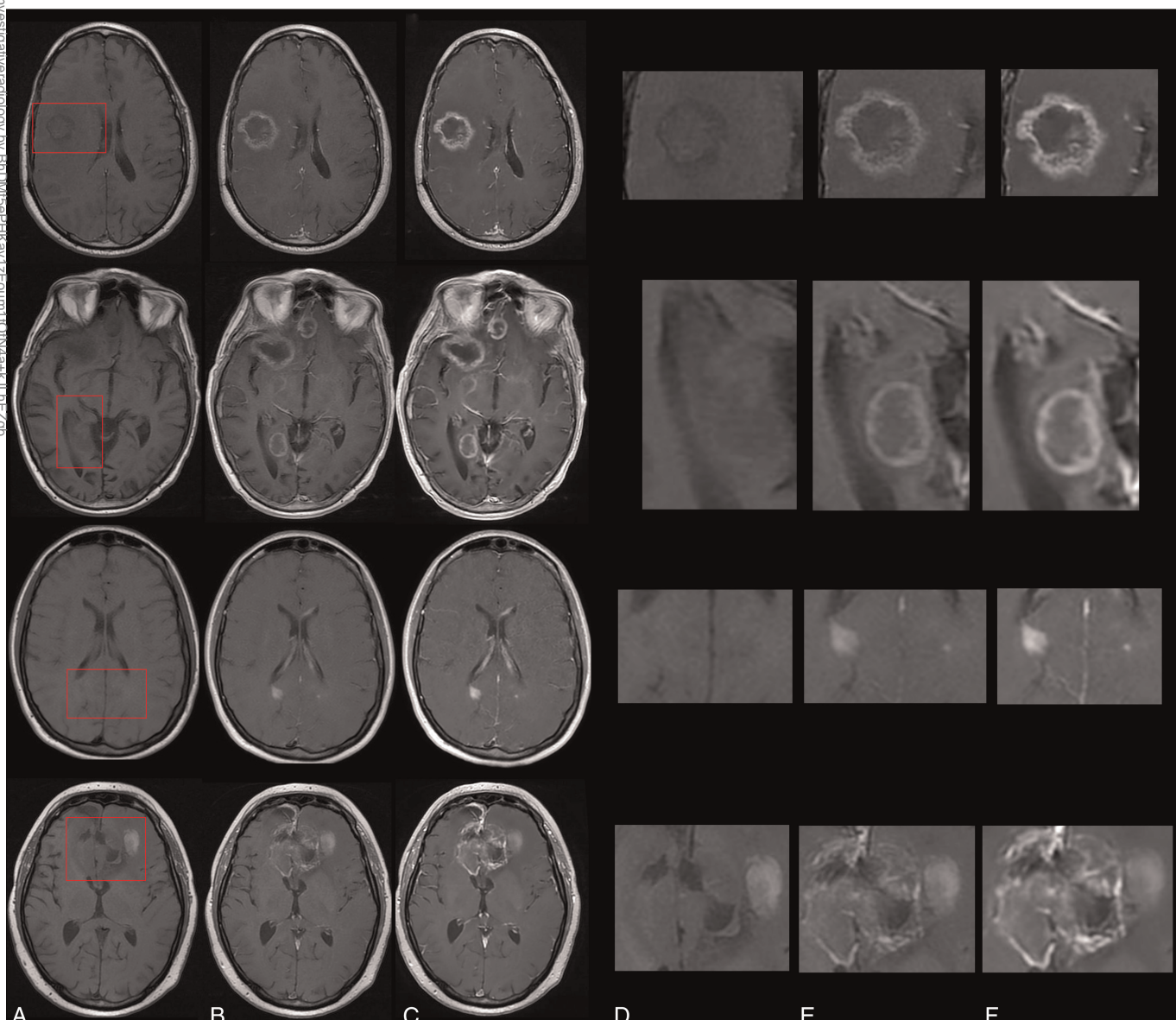
FIGURE 8. Representative clinical cases of astrocytoma, metastases, multiple sclerosis, and glioblastoma, respectively, from top to bottom. A and D, Pre-CA. B and E, Standard dose postcontrast image. C and F, Virtual double-dose image. The red square indicates the zoomed area showed in panels D, C, and F.

FIGURE 9. Contrast evaluations using quantitative nonsubjective metrics (%CNR and %LBR) of virtual double-dose images compared against standard-dose acquisitions on testing data sets.

preclinical study using an animal model of brain tumor. This study enabled us to fine-tune the model hyperparameters by comparing the virtual contrast images with ground-truth double-dose images that may not be available in the clinical database. In addition, we were able to confirm our hypothesis that the trained network can reliably predict the contrast that would occur from a double CA dose when applied to standard-dose images.

For the present study, we chose to focus on contrast enhancement of brain lesions. Besides the obvious clinical relevance of brain neoplastic and metastatic disease, a largely unmet medical need, the choice was driven by the favorable characteristics of neuroimaging data. From a technical point of view, brain MR images are less affected by susceptibility and motion artifacts than, for example, abdominal images, and can present a broad variety of lesions, with different size, definition, conspicuity, and CA uptake. Hence, brain images are less prone to artifacts and offer an ideal arena for the implementation and validation of our training approach.

For the preclinical study, a model of brain glioma based on implantation of C6 cells was selected. C6 cells grow intracerebrally in Wistar rats forming tumors that mimic several characteristics of malignant human glioma including nuclear pleomorphism, high mitotic index, foci of tumor necrosis and intratumoral hemorrhage, parenchymal invasion, diffuse infiltrative borders, and palisading cells surrounding areas of necrosis.[11,47,48] Hence, this model offers a variety of features that facilitate generalization of the method to detection of a variety of lesions.

Two different metrics, PSNR and SSIM, were chosen for the comparison of virtual contrast and ground-truth images in the preclinical study. Peak signal-to-noise ratio is a standard metric based on MSE, which estimates the errors between images. Structural similarity index measures the perceptual difference between 2 images and ranges between −1 and 1 (1 for identical images). Quantitative analysis of the preclinical virtual double-dose contrast images shows significant improvement over the standard-dose and a high degree of similarity to the double-dose ground-truth for both metrics. We report a difference of PSNR of 1 dB (at 7 T) and 0.3 dB (at 3 T), and SSIM values of 0.91 (double dose vs virtual double dose) and 0.90 (standard dose vs double dose). For comparison, in a clinical study where experimental data were used to predict standard-dose images from low-dose images, Gong at al[6] reported lower absolute SSIM values (0.76 low dose vs standard dose vs 0.85 synthesized full dose vs standard dose) and higher PSNR values (5 dB). However, substantial differences between Gong's study and ours should be noted. First, a much larger amplification factor (k = 5) was investigated in Gong's study. Moreover, in our study, quantitative comparison of predicted and experimental double-dose images was performed on the entire field of view, which includes skull and extracranial tissues. Although our results clearly indicate a statistically significant improvement of the predicted double-contrast over standard-dose images, the overall sensitivity of our metrics was reduced due to the inclusion of nonenhancing tissues (eg, muscle) outside the brain within the image. This is a conservative choice that reduces the measured

The qualitative assessment in terms of visibility, degree of delineation, and brightness of small low-enhancing lesions was performed in a subset of 30 patients, 15 of whom affected by multiple sclerosis and the remaining by multiple metastases. As detailed in Table 4, the virtual double-dose images were preferred by all 3 readers. On average between readers, standard-dose images were graded 3.51 of 5 (average to good), whereas virtual double-dose images were graded 4.46 of 5 (good to excellent). Two representative examples of small lesion virtually enhanced by our model are shown in Figure 10.

DISCUSSION

In this study, we have implemented and assessed a training strategy that uses synthetic data to enhance the image contrast of GBCAs in diagnostic MR images. The proposed approach involves using synthetic half-dose images to train the model to virtually double the CA dose, and then applying the trained network to standard images to produce virtual image contrast equivalent to double the standard dose. To optimize the model and verify the strategy, we conducted a dedicated

TABLE 3. Average Scores of CE, DC, AS, and IQ for the Selected Test Sample (n = 60 Standard Dose and n = 60 Virtual Double Dose)

Reader ID	CE		DC		AS		IQ	
	Standard Dose	**Virtual Double Dose**	**Standard Dose**	**Virtual Double Dose**	**Standard Dose**	**Virtual Double Dose**	**Standard Dose**	**Virtual Double Dose**
Reader 1	3.92 (3.8, 4.1)	3.85 (3.7, 4.0)	3.92 (3.7, 4.1)	3.33 (3.1, 3.6)	3.30 (3.1, 3.5)	2.45 (2.2, 2.7)	3.95 (3.8, 4.1)	3.15 (2.9, 3.4)
Reader 2	3.50 (3.2, 3.8)	4.02 (3.8, 4.3)	3.62 (3.4, 3.9)	3.40 (3.2, 3.6)	3.58 (3.3, 3.8)	3.17 (2.9, 3.4)	3.83 (3.6, 4.1)	3.45 (3.2, 3.7)

Grades are expressed on a 5-point Likert scale ranging from 1 (poor) to 5 (excellent). Mean values are reported, with the corresponding standard deviations between parentheses.

TABLE 4. Average Scores of Visibility, Delineation, and Brightness of Small Contrast Enhancing Lesion for the 30 Cases of the Selected Test Sample

	Standard Dose	Virtual Double Dose	Standard Dose vs Virtual Double Dose	Counts
Reader average	3.51 (0.62)	4.46 (0.69)	$P \ll 0.001$*	90
Reader 1	3.67 (0.55)	4.63 (0.56)	$P \ll 0.001$*	30
Reader 2	3.63 (0.61)	4.63 (0.61)	$P \ll 0.001$*	30
Reader 3	3.23 (0.63)	4.10 (0.76)	$P \ll 0.001$*	30
R1 vs R2	$P = 0.77$	$P = 1$	NA	30
R1 vs R3	$P < 0.05$*	$P < 0.001$*	NA	30
R2 vs R3	$P < 0.05$*	$P < 0.01$*	NA	30

Grades are expressed on a 5-point Likert scale ranging from 1 (poor) to 5 (excellent). Mean values are reported, with the corresponding standard deviations between parentheses. Best metrics are shown in bold when the 5% significance threshold is met. *Differences across readers and postcontrast MRI sequences are compared using 2-tailed t tests, and P values are reported.

effect size, but does not require operator- or algorithm-based segmentation procedures, thus avoiding potential biases.

Interestingly, the performance of our approach was different at the 2 magnetic field strengths used for the preclinical study (3 T and 7 T). The difference may be attributed to multiple factors. Beyond magnetic field strength, the 2 scanners used for data collection differ in coil configuration (surface vs volume coils at 3 T and 7 T, respectively). Moreover, the relaxivity of GBCA is slightly different at the 2 magnetic field strengths (3.46 vs 3.35 mM^{-1} s^{-1} at 3 T and 7 T, respectively, Shen et al[49]). Finally, the different SNR in the 2 sets of images may have contributed to determine different predictive powers.

The contrast amplification effect of the trained and optimized network was assessed both quantitatively and qualitatively on a large clinical data set. As expected, a significant increment in contrast was observed in lesions but was also apparent in blood vessels, thus increasing visibility of vascular network. As these are generally anatomically distinct from pathology, and as such easy to recognize, their more prominent appearance is unlikely to affect radiological assessment. A slight loss of anatomical details in the nonenhancing regions (ie, brain parenchyma) was reported by all readers. Flattening of gray levels in gray and white matter is sometimes observed after administration of the CA,[19] possibly due to the different densities of capillaries in the 2 tissues.[50]

Virtual amplification of contrast seems to exacerbate this effect, consistent with differential increase of contrast in gray and white matter.

Contrast amplification is thus far achieved by increasing CA dose to enhance lesion detection.[5,51] In brain metastases for instance, in particular when there are multiple lesions present, a better delineation and conspicuity of smaller lesions has an impact on the treatment plan decision. Engh et al[52] reported 29% additional metastases with double-dose imaging performed for radiotherapy planning; more importantly, this changed the treatment plan in 89% of patients.

In the present study, we applied our strategy to simulate contrast corresponding to a virtual double-dose of CA. However, the approach of generating synthetic data makes it possible to modulate the dose amplification factor and to train the model to predict contrast at GBCA doses several times larger than those used in the clinical practice. Although this possibility has not been explored here in full, it represents an avenue of further development for our approach.

The present study has potential limitations listed hereafter. Coregistration of precontrast and postcontrast images is part of the preprocessing step in our procedure. A not proper coregistration may cause artifacts that can influence (without compromising) the quality of the half-dose images simulated through a mathematical function calculated voxel-wise. Thus, if the voxel correspondence between precontrast and postcontrast images is poor, application of standard coregistration
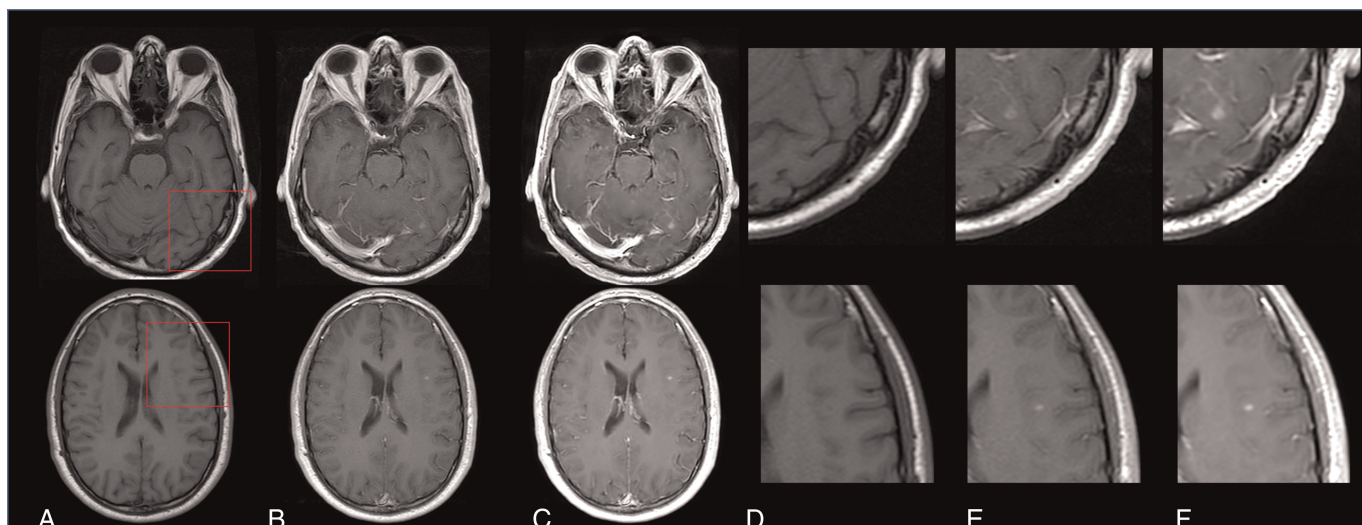
FIGURE 10. Representative clinical cases of metastases and multiple sclerosis first and second row, respectively. A and D, Pre-CA. B and E, Standard dose post contrast image. C and F, Virtual double-dose image. The red square indicates the zoomed area showed in panels D, C, and F.

algorithms may not suffice, and artifacts similar to motion artifact or partial volume effect might occur. In this study, we excluded by visual inspection approximately 15% of the patient cohort due to evident misalignment of precontrast and postcontrast acquisitions. The percentage is rather high, and it could be significantly reduced using more sophisticated coregistration techniques that are already part of the state of the art but are not object of the present study. A potential solution to work around the misalignment of images applied for training has been proposed by Haubold et al,[53] where the CycleGAN architecture is applied to abdominal computed tomography in a large animal model. Since CycleGAN loss does not contain any pixelwise computation, the training is not affected by coregistration imperfections.

Finally, despite the large number of magnetic field strengths and the different scanners included in the present study, we note that the clinical study was by nature monocentric. Further retrospective multicentric studies may be useful to strengthen the results presented here, and to test generalizability of the proposed AI tool to other clinical contexts.

CONCLUSIONS

In conclusion, the present study proposes a DL approach based on synthetic training data to boost image contrast in CA-enhanced MR images. Specifically, we leveraged a physical model to simulate different levels of MR contrast from a gadolinium-based MR CA, and we applied the resulting data sets to train a neural network to predict contrast at a GBCA dose that was double the one normally used in the clinical practice. Preclinical data from a specially designed study were used to determine the optimal hyperparameters and to optimize the model against ground-truth data.

The approach was then applied to amplify contrast in a broad set of clinical data from subjects with a variety of central nervous system lesions. Blind reading by expert neuroradiologists demonstrates that the virtual contrast improves qualitatively and quantitatively delineation of lesion boundaries and visibility of vascular network compared with standard-dose images. The proposed AI tool proves particularly effective in increasing detectability of small, low-enhancing lesion (eg, small metastasis or multiple sclerosis plaques).

REFERENCES

1. Gil B, Hwang EJ, Lee S, et al. Detection of leptomeningeal metastasis by contrast-enhanced 3D T1-SPACE: comparison with 2D FLAIR and contrast-enhanced 2D T1-weighted images. *PloS One*. 2016;11:e0163081.
2. Harris P, Diouf A, Guilbert F, et al. Diagnostic reliability of leptomeningeal disease using magnetic resonance imaging. *Cureus*. 2019;11:e4416.
3. Kaufmann TJ, Smits M, Boxerman J, et al. Consensus recommendations for a standardized brain tumor imaging protocol for clinical trials in brain metastases. *Neuro Oncol*. 2020;22:757–772.
4. Subedi KS, Takahashi T, Yamano T, et al. Usefulness of double dose contrast enhanced magnetic resonance imaging for clear delineation of gross tumor volume in stereotactic radiotherapy treatment planning of metastatic brain tumors: a dose comparison study. *J Radiat Res*. 2013;54:135–139.
5. Van Dijk P, Sijens PE, Schmitz PI, et al. Gd-enhanced MR imaging of brain metastases: contrast as a function of dose and lesion size. *Magn Reson Imaging*. 1997;15:535–541.
6. Runge VM, Kirsch JE, Burke VJ, et al. High-dose gadoteridol in MR imaging of intracranial neoplasms. *J Magn Reson Imaging*. 1992;2:9–18.
7. Lohrke J, Berger M, Frenzel T, et al. Preclinical profile of gadoquatrane: a novel tetrameric, macrocyclic high relaxivity gadolinium-based contrast agent. *Invest Radiol*. 2022;57:629–638.
8. Deike-Hofmann K, Thünemann D, Breckwoldt MO, et al. Sensitivity of different MRI sequences in the early detection of melanoma brain metastases. *PloS One*. 2018;13:e0193946.
9. Filippi M, Yousry T, Campi A, et al. Comparison of triple dose versus standard dose gadolinium-DTPA for detection of MRI enhancing lesions in patients with MS. *Neurology*. 1996;46:379–384.
10. Rovaris M, Mastronardo G, Prandini F, et al. Short-term evolution of new multiple sclerosis lesions enhancing on standard and triple dose gadolinium-enhanced brain MRI scans. *J Neurol Sci*. 1999;164:148–152.
11. Rovaris M, Rodegher M, Comi G, et al. Correlation between MRI and short-term clinical activity in multiple sclerosis: comparison between standard- and triple-dose Gd-enhanced MRI. *Eur Neurol*. 1999;41:123–127.
12. Su X, Kong X, Lu Z, et al. Use of magnetic resonance neurography for evaluating the distribution of chronic inflammatory demyelinating polyneuropathy. *Korean J Radiol*. 2020;21:483–493.
13. Chaudhary V, Bano S. Imaging of the pituitary: recent advances. *Indian J Endocrinol Metab*. 2011;15 Suppl 3(Suppl3):S216–S223.
14. Zimny A, Sasiadek M. Contribution of perfusion-weighted magnetic resonance imaging in the differentiation of meningiomas and other extra-axial tumors: case reports and literature review. *J Neurooncol*. 2011;103:777–783.
15. Kanda T, Ishii K, Kawaguchi H, et al. High signal intensity in the dentate nucleus and globus pallidus on unenhanced T1-weighted MR images: relationship with increasing cumulative dose of a gadolinium-based contrast material. *Radiology*. 2014;270:834–841.
16. McDonald RJ, McDonald JS, Kallmes DF, et al. Intracranial gadolinium deposition after contrast-enhanced MR imaging. *Radiology*. 2015;275:772–782.
17. Finck T, Gempt J, Zimmer C, et al. MR imaging by 3D T1-weighted black blood sequences may improve delineation of therapy-naive high-grade gliomas. *Eur Radiol*. 2021;31:2312–2320.
18. Bapst B, Amegnizin JL, Vignaud A, et al. Postcontrast 3D T1-weighted TSE MR sequences (SPACE, CUBE, VISTA/BRAINVIEW, isoFSE, 3D MVOX): technical aspects and clinical applications. *J Neuroradiol*. 2020;47:358–368.
19. Hao J, Bourrinet P, Desché P. Assessment of pharmacokinetic, pharmacodynamic profile, and tolerance of gadopiclenol, a new high relaxivity GBCA, in healthy subjects and patients with brain lesions (phase I/IIa study). *Invest Radiol*. 2019;54:396–402.
20. Robic C, Port M, Rousseaux O, et al. Physicochemical and pharmacokinetic profiles of gadopiclenol: a new macrocyclic gadolinium chelate with high T1 relaxivity. *Invest Radiol*. 2019;54:475–484.
21. Gong E, Pauly JM, Wintermark M, et al. Deep learning enables reduced gadolinium dose for contrast-enhanced brain MRI. *J Magn Reson Imaging*. 2018;48:330–340.
22. Pasumarthi S, Tamir JI, Christensen S, et al. A generic deep learning model for reduced gadolinium dose in contrast-enhanced brain MRI. *Magn Reson Med*. 2021;86:1687–1700.
23. Zaharchuk G, Gong E, Wintermark M, et al. Deep learning in neuroradiology. *AJNR Am J Neuroradiol*. 2018;39:1776–1784.
24. Luo H, Zhang T, Gong NJ, et al. Deep learning–based methods may minimize GBCA dosage in brain MRI. *Eur Radiol*. 2021;31:6419–6428.
25. Haase R, Pinetz T, Kobler E, et al. Artificial contrast: deep learning for reducing gadolinium-based contrast agents in neuroradiology. *Invest Radiol*. 2023;Publish Ahead of Print. doi:10.1097/RLI.0000000000000963. Online ahead of print.
26. Haase R, Pinetz T, Bendella Z, et al. Reduction of gadolinium-based contrast agents in MRI using convolutional neural networks and different input protocols: limited interchangeability of synthesized sequences with original full-dose images despite excellent quantitative performance. *Invest Radiol*. 2023;58:420–430. doi: 10.1097/RLI.0000000000000955. Online ahead of print.
27. Pasquini L, Napolitano A, Pignatelli M, et al. Synthetic post-contrast imaging through artificial intelligence: clinical applications of virtual and augmented contrast media. *Pharmaceutics*. 2022;14:2378.
28. Bone A, Ammari S, Menu Y, et al. From dose reduction to contrast maximization: can deep learning amplify the impact of contrast media on brain magnetic resonance image quality? A reader study. *Invest Radiol*. 2022;57:527–535.
29. Arvanitis TN, White S, Harrison S, et al. A method for machine learning generation of realistic synthetic datasets for validating healthcare applications. *Health Informatics J*. 2022;28:14604582221077000.
30. Chen RJ, Lu MY, Chen TY, et al. Synthetic data in machine learning for medicine and healthcare. *Nat Biomed Eng*. 2021;5:493–497.
31. Haubold J, Hosch R, Umutlu L, et al. Contrast agent dose reduction in computed tomography with deep learning using a conditional generative adversarial network. *Eur Radiol*. 2021;31:6087–6095.
32. Müller-Franzes G, Huck L, Tayebi Arasteh S, et al. Using machine learning to reduce the need for contrast agents in breast MRI through synthetic images. *Radiology*. 2023;21:e222211.

33. Lee D, Yoo J, Ye JC, et al. Deep artifact learning for compressed sensing and parallel MRI. In: *2017 IEEE 14th International Symposium on Biomedical Imaging (ISBI 2017)*. 2017:15–18.

34. Gabrielsson J, Weiner J. *Pharmacokinetic & Pharmacodynamic—Data Analysis: Concepts and Applications*. 4th ed. Stockholm, Sweden: Swedish Pharmaceutical Press; 2007.

35. Tofts PS. Modeling tracer kinetics in dynamic Gd-DTPA MR imaging. *J Magn Reson Imaging*. 1997;7:91–101.

36. Tofts PS, Brix G, Buckley DL, et al. Estimating kinetic parameters from dynamic contrast-enhanced T1-weighted MRI of a diffusable tracer: standardized quantities and symbols. *J Magn Reson Imaging*. 1999;10:223–232.

37. Tofts PS, Kermode AG. Measurement of the blood-brain barrier permeability and leakage space using dynamic MR imaging. 1. Fundamental concepts. *Magn Reson Med*. 1991;17:357–367.

38. Grobben B, De Deyn PP, Slegers H. Rat C6 glioma as experimental model system for the study of glioblastoma growth and invasion. *Cell Tissue Res*. 2002;310:257–270.

39. Robert P, Vives V, Grindel AL, et al. Contrast-to-dose relationship of gadopiclenol, an MRI macrocyclic gadolinium-based contrast agent, compared with gadoterate, gadobenate, and gadobutrol in a rat brain tumor model. *Radiology*. 2020;294:117–126.

40. OECD, Guidance document on the recognition, assessment, and use of clinical signs as humane endpoints for experimental animals used in safety evaluation. In: OECD Series on Testing and Assessment. Paris, France: OECD Publishing; 2002.

41. Marstal K, Berendsen F, Staring M, et al. SimpleElastix: a user-friendly, multi-lingual library for medical image registration. In: *IEEE Conference on Computer Vision and Pattern Recognition Workshops (CVPRW)*. 2016:574–582.

42. Gudbjartsson H, Patz S. The Rician distribution of noisy MRI data. *Magn Reson Med*. 1995;34:910–914.

43. Seitzer M, Yang G, Schlemper J, et al. Adversarial and perceptual refinement for compressed sensing MRI reconstruction. In: Frangi A, Schnabel J, Davatzikos C, et al, eds. *Medical Image Computing and Computer Assisted Intervention. Lecture Notes in Computer Science*. MICCAI; 2018:11070.

44. Simonyan K, Zisserman A. *Very Deep Convolutional Networks for Large-Scale Image Recognition*. International Conference on Learning Representations; 2015.

45. Sara U, Akter M, Uddin M. Image quality assessment through FSIM, SSIM, MSE and PSNR—a comparative study. *J Comput Commun*. 2019;7:8–18.

46. Horé A, Ziou D. Image quality metrics: PSNR vs. SSIM. In: *2010 20th International Conference on Pattern Recognition*. 2010:2366–2369.

47. Kemerli C, Taskin MM, Sutpideler N, et al. Histopathology, invasion, migration and tumorigenicityin the C6 rat glioma model. *Turk Neurosurg*. 2005;15:109–115.

48. Day SE, Kettunen MI, Cherukuri MK, et al. Detecting response of rat C6 glioma tumors to radiotherapy using hyperpolarized [1- 13C]pyruvate and 13C magnetic resonance spectroscopic imaging. *Magn Reson Med*. 2011;65:557–563.

49. Shen Y, Goerner FL, Snyder C, et al. T1 relaxivities of gadolinium-based magnetic resonance contrast agents in human whole blood at 1.5, 3, and 7 T. *Invest Radiol*. 2015;50:330–338.

50. Kubíková T, Kochová P, Tomášek P, et al. Numerical and length densities of microvessels in the human brain: correlation with preferential orientation of microvessels in the cerebral cortex, subcortical grey matter and white matter, pons and cerebellum. *J Chem Neuroanat*. 2018;88:22–32.

51. Kim ES, Chang JH, Choi HS, et al. Diagnostic yield of double-dose gadobutrol in the detection of brain metastasis: intraindividual comparison with double-dose gadopentetate dimeglumine. *AJNR Am J Neuroradiol*. 2010;31:1055–1058.

52. Engh JA, Flickinger JC, Niranjan A, et al. Optimizing intracranial metastasis detection for stereotactic radiosurgery. *Stereotact Funct Neurosurg*. 2007;85:162–168.

53. Haubold J, Jost G, Theysohn JM, et al. Contrast media reduction in computed tomography with deep learning using a generative adversarial network in an experimental animal study. *Invest Radiol*. 2022;57:696–703.